NANO · MICRO small
www.small-journal.com

Electrochemical Self-Healing Nanocrystal Electrodes for Ultrastable Potassium-Ion Storage

*Wei-Cheng Lin, Yi-Chun Yang, and Hsing-Yu Tuan**

The unique properties of self-healing materials hold great potential in battery systems, which can exhibit excellent deformability and return to its original shape after cycling. Herein, a Cu_3BiS_3 anode material with self-healing mechanisms is proposed for use in ultrastable potassium-ion battery (PIB) and potassium-ion hybrid capacitor (PIHC). Different from the binder design, Cu_3BiS_3 anode can exhibit the dual advantages of phase and morphological reversibility, further remaining original property after potassiation/depotassiation and exhibiting ultrastable cycling performance. The reversible electrochemical reconstruction during the continuous charge/discharge processes is beneficial to maintain the structure and function of the material. Furthermore, the conversion reactions during the charge and discharge process produce two advantages: i) suppressing the shuttle effect due to the formation of the heterostructure interface between Cu (111) and Bi (012); ii) Cu can avoid the agglomeration of Bi nanoparticles (NPs), further improving the electrochemical performance and long-cycle stability of the Cu_3BiS_3 electrode. As a result, the Cu_3BiS_3 electrode not only exhibits a long cycle life in half cells, but also 2000 cycles and 12000 cycles in PIB and PIHC full cells, respectively.

1. Introduction

In recent years, energy storage devices have attracted extensive attention due to the demand for ecosystem and economic development. Lithium-ion batteries (LIBs) have been proven to be the most practical energy storage device due to high energy density, high operating voltage, and long cycle life.[1] However, the low abundance of lithium resources (0.0017%) seriously hinders its further application.[2] Therefore, sodium-ion batteries (SIBs) and potassium-ion batteries (PIBs) have also been proposed as alternatives because of abundant sodium and potassium resources, high specific capacity and long cycling stability, etc.[3] It is worth noting that PIB is considered as a candidate of next-generation non-lithium ion energy storage system due to abundant potassium resources and low redox potential K/K^+ (−2.93 V) similar to Li/Li^+ (−3.04 V). However, the radius of K^+ (1.38 Å) is larger than that of Li^+ (0.76 Å), so that the electrode is more prone to structure collapse under repeated K^+ insertion and extraction during the potassiation/depotassiation process.[4] In terms of anodes, three types of materials have attracted extensive attention: intercalation-type, conversion-type, and alloying-type, where conversion-type and alloy-type anodes can achieve higher energy densities and wider voltage plateaus compared with intercalation-type anodes. However, conversion-type and alloy-type anode materials usually have irreversible reactions during potassiation/depotassiation. Their practical use is limited to a huge degree of volume change because the structural collapse of electrode is unavoidable due to the intercalation of a large amount of K-ions, resulting in irreversible capacity loss and material pulverization, which in turn has a huge impact on battery performance.[5,6] To improve cycle-life, rate performance, or ion diffusion/adsorption, it is necessary to develop new composite materials, optimize structural design of materials, or adapt materials with self-healing ability to reduce electrode damage.[7–9]

Self-healing is broadly defined as the tendency of a system to correct any disturbances and stimuli from external factors due to the inherent mechanisms in its nature. In biological systems, they can self-repair where they are damaged through a complex set of biochemical programs. The most common self-healing material is the skin, which automatically heal the wound to restore the function of the normal tissue after injury. In recent years, the concept of self-healing has been gradually developed in battery systems.[10,11] Electrode materials suffer from mechanical fracture problems due to repeated ion insertion/extraction of the battery. By imitating the self-healing ability of biological systems, electrode composites can greatly extend the lifespan of energy storage devices and restore the corresponding electrochemical performance. For example, the self-healing binders, including self-healing poly(ether-thioureas) (SHPET), bifunctional polyurethane (BFPU), poly(acrylic acid)-poly(2-hydroxyethyl acrylate-co-dopamine methacrylate) (PAA-P(HEA-co-DMA)) and polyethylene glycol (PEG) groups incorporated into the self-healing polymer (SHP-PEG) have attracted much attention due to their superior ability to repair cracks caused by volume changes in anodes compared to conventional binders (e.g., polyvinylidene fluoride (PVDF), sodium carboxymethyl cellulose (NaCMC)). Chen et al. found that hydrogen bonded pairs realize the repair function of self-healing polymer binder so as to accommodate large volume

W.-C. Lin, Y.-C. Yang, H.-Y. Tuan
Department of Chemical Engineering
National Tsing Hua University
Hsinchu 30013, Taiwan
E-mail: hytuan@che.nthu.edu.tw

The ORCID identification number(s) for the author(s) of this article can be found under https://doi.org/10.1002/smll.202300046.

DOI: 10.1002/smll.202300046

change.[12–15] The silicon anode using self-healing binder exhibits excellent rate capability (1917 mA h g^{-1} at 4.2 A g^{-1}) and good cycling stability (250 cycles at 4.2 A g^{-1}).[12] On the other hand, several materials can achieve mechanical self-healing effects through the reversible solid-liquid transition of liquid metals. Zhu et al. reported a lithium anode made of core-shell containing liquid metal (Ga) active materials showing high surface tension, fluidity, and electrical conductivity exhibits high capacity (603.9 mA h g^{-1} at 1000 mA g^{-1}).[16] Different from the properties of crack repairing, Haghighat-Shishavan et al. found that the $Sn_2P_2S_6$-CNT hybrid anode has reversible self-healing and regeneration properties during the charge and discharge process.[17] However, to the best of our knowledge, there are rare examples of self-healing anode materials, especially for PIBs.

Conversion-type or alloy-type materials undergo significant morphological and structural evolution after cycling, resulting in the poor electrochemical battery performance.[18,19] Intercalation-type materials with a strong framework facilitate the ion intercalation/deintercalation of ions, thereby imparting low volume change. However, due to its limited interstitial sites, intercalation-type material is insufficient to meet the needs of high-capacity batteries.[20] Conversely, although conversion-type and alloy-type anodes can exhibit high capacity, they are also accompanied by huge volume changes during potassiation/depotassiation. The morphological changes induced by electrochemical activation during cycling can be divided into two types: 1) electrochemical sintering, i.e., aggregation of NPs into larger sized particles; 2) electrochemical reconstruction, i.e., in situ assembly of active material into new favorable structures. Electrochemical reconstruction is generally considered to be beneficial to maintain battery performance, whereas electrochemical sintering can destroy electrode integrity. Interestingly, according to many reports related to electrochemical reconstruction, it can be found that most of the materials are reconstructed small-grained materials from large-grained materials. Ni et al. found that Li_3VO_4 aggregates gradually transform into nanocrystals after a continuous charge and discharge process, which in turn creates good contacts with carbon nanosheets, thus improving high Li-ion storage and stability.[21] In addition, Ni et al. also found that the Cu_3P dots is well embedded in the carbon matrix, triggering improved electrochemical performance.[22] Chen et al., on the other hand, found that the in situ formation of submicron BiSb nanocrystalline aggregates after potassiation/depotassiation, where the interconnected NP structure effectively reduces the effects of severe volume changes,[23] and provides an efficient K^+ diffusion pathway, better electron transport to achieve highly reversible potassium ion storage. However, there is a problem of agglomeration of small particle materials during the charging and discharging process, and most of them need to design a carbon framework to achieve separation efficiency.

In this study, we develop a Cu_3BiS_3 anode material with dual reversible advantages for the intrinsic (phase change) and extrinsic (morphology) in PIB. We propose a self-healing mechanism to understand the evolution of Cu_3BiS_3 anodes during potassiation/depotassiation (**Scheme 1**). The self-healing process is as follows: when discharged to 0.01 V, the large-grained Cu_3BiS_3 NPs will transform into the small-grained intermediates (Cu, K_3Bi, and K_2S). When charged to 1.6 V, the Cu/Bi heterostructure interface is formed, which can suppress the shuttle effect. And, Cu can be used as a separator to avoid the serious aggregation of Bi particles, which is beneficial to

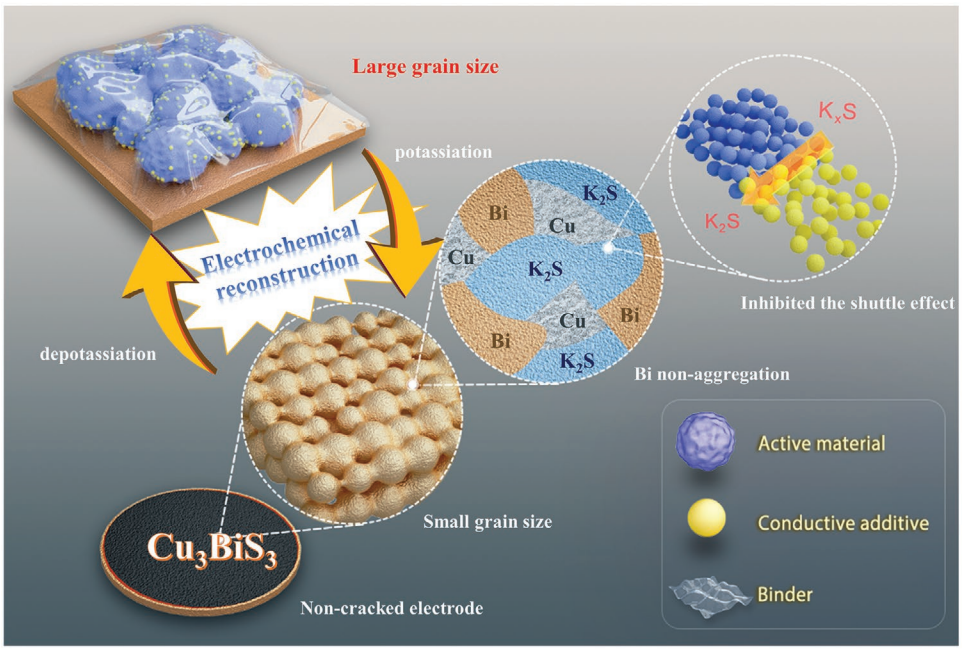

Scheme 1. Schematic diagram of the self-healing process and effect of the Cu_3BiS_3 nanocrystal potassium ion electrode. Electrochemical reconstruction promotes the dual properties (phase and morphology reversibility) of Cu_3BiS_3 anode, which are beneficial for producing the noncracked electrode due to low bond energy (Cu—S and Bi—S bond energies) and small bulk modulus: transformation between Cu_3BiS_3 with large grain size and intermediates with small grain size. Intermediates are good for high stability during the potassiation/depotassiation process because Cu can avoid the aggregation of Bi particles and Cu/Bi heterostructure interface can inhibit the shuttle effect.

improve the kinetics of Cu_3BiS_3. Finally, when charged to 3 V, the small-grained intermediates will return to large-grained Cu_3BiS_3 NPs again. The self-healing mechanism is stably repeated in the subsequent cycles, even up to 2000 cycles, and promotes to the reversible reconstruction of Cu_3BiS_3 NPs, effectively alleviating the crack of electrode materials caused by ion intercalation/intercalation. Through the self-healing property, it can achieve higher quality and longer cycle life. The Cu_3BiS_3 electrode exhibits a long cycle life of 2000 cycles with a stable capacity at 500 mA g^{-1}. It is worth noting that based on density functional theory (DFT) calculations: 1) the high K_2S_5 adsorption energy of Cu/Bi heterostructure interface, 2) the low bond energy and low energy barrier of Cu_3BiS_3 and 3) the low modulus of Cu_3BiS_3, we further provide the basic theory of the function of self-healing Cu_3BiS_3. Finally, through PIB and PIHC full cells tests, we evaluate the feasibility of Cu_3BiS_3 anodes in advanced storage systems.

2. Results and Discussion

Cu_3BiS_3 NPs was obtained by a simple hydrothermal synthesis,[24] as illustrated in **Figure 1**a. First, after CuCl was dissolved in ethylenediamine, $Bi(NO_3)_3 \cdot 5H_2O$ was added to form a dark blue solution (solution A). Next, the sulfur powder was dissolved in ethylenediamine to form solution B. The solution B was slowly dropped into the solution A. After a uniform mixed solution was achieved, it was transferred into the reactor and heated to 180 °C for 12 h. Subsequently, the final product can be obtained. Scanning electron microscopy (SEM) image and transmission electron microscope (TEM) image show the spherical and irregularly shaped Cu_3BiS_3 NPs with a grain size of ≈100 nm (Figure 1b,c and Figure S1, Supporting Information). The selected area electron diffraction (SAED) images further confirmed the good crystallinity and single-crystal properties of the as-prepared Cu_3BiS_3 (Figure 1d). High-resolution TEM (HRTEM) images of Cu_3BiS_3 NPs showed clear lattice fringes (Figure 1e). Fast Fourier transform (FFT) analysis indicates good crystallinity and reveals lattice fringes with a spacing of 0.322 nm and 0.285 nm corresponding to the (1 2 1) and (1 1 3) planes of Cu_3BiS_3 (Figure 1f,g). The energy-dispersive X-ray spectroscopy (EDS) mapping images indicate a uniform distribution of Cu, Bi, and S elements (Figure 1h). The XRD pattern of Cu_3BiS_3 is shown in Figure 1i. All diffraction peaks are well indexed to the orthorhombic structure of Cu_3BiS_3 (PDF#00-043-1479), indicating successfully synthesized the high-purity Cu_3BiS_3. The N_2 adsorption–desorption curve of the Cu_3BiS_3 has no obvious hysteresis loop, which resembles type II adsorption isotherm, indicating that this material has no mesoporous or hollow structures (Figure S2, Supporting Information). X-ray photoelectron spectroscopy (XPS) was used to reveal the composition and chemical state of Cu_3BiS_3 (Figure 1j,k and Figure S3, Supporting Information). Figure 1j shows the high-resolution Cu 2p spectrum. Two peaks are observed at 952.0 and 932.2 eV, which can be attributed to Cu $2p_{3/2}$ and Cu $2p_{1/2}$.[25–27] The high-resolution Bi 4f and S 2p spectrums are shown in Figure 1k, two peaks are observed at 163.0 eV and 157.7 eV, corresponding to Bi $4f_{5/2}$ and Bi $4f_{7/2}$,[28] respectively. In addition, the small peaks located to the left of Bi $4f_{5/2}$ and Bi $4f_{7/2}$ can be indexed to Bi_2O_3 $4f_{5/2}$ (at around 164.2 eV) and Bi_2O_3 $4f_{7/2}$ (at around 158.9 eV), which can be attributed to the oxides formed on the surface.[29] The peaks located at 161.1 eV and 162.1 eV correspond to S $2p_{3/2}$ and S $2p_{1/2}$.[30] Therefore, the Cu^+, Bi^{3+} and S^{2-} valence states of the obtained Cu_3BiS_3 are confirmed through the XPS analysis.

The electrochemical behaviors of the Cu_3BiS_3 electrode were investigated (**Figure 2**). First, the cyclic voltammetry (CV) of Cu_3BiS_3 electrode was carried out in the voltage of 0.01–3.0 V (vs K^+/K) at a scan rate of 0.1 mV s^{-1} in the first three cycles (Figure 2a). During the first potassiation process, the weak reduction peak around 1.1 V appeared, which is weakened during the subsequent cycles, which was attributed to conversion reaction from Cu_3BiS_3 to Cu, Bi and K_xS_y, the alloying reaction between Bi and K^+ ($Bi \rightarrow KBi_2$), and the formation of the solid electrolyte interface (SEI).[31] Then, the broad reduction peak centered at 0.7 V can be attributed to the alloying reaction from KBi_2 to K_3Bi_2 and the conversion reaction between K_xS_y and K^+.[32] The reduction peak at 0.1 V can be attributed to the conversion reaction from K_xS_y to K_2S, and the alloying reaction from K_3Bi_2 to K_3Bi. In contrast, during the first depotassiation process, the oxidation peak at 0.6 and 0.8 V corresponds to the dealloying reaction from K_3Bi to KBi_2 and the conversion reaction of K_xS_y. The oxidation peak at 1.3 V corresponds to the dealloying process ($KBi_2 \rightarrow Bi$) and the conversion reaction of K_xS_y.[33] Finally, the third oxidation peak at 2.4 V is attributed to the conversion of Cu, Bi and K_xS_y to Cu_3BiS_3.[34] In the subsequent cycles, the CV curves are almost overlapped, indicating the good reversibility of the electrochemical reaction. Figure 2b shows the galvanostatic charge-discharge voltage curves of the Cu_3BiS_3 electrode at 50 mA g^{-1} in the first three cycles. The initial discharge and charge capacity of the Cu_3BiS_3 electrode are 551 and 385 mA h g^{-1}, respectively. The corresponding initial Coulombic efficiency (ICE) is about 69.8%. Furthermore, the galvanostatic charge/discharge (GCD) curves of the second and third almost overlap, proving the high reversibility of the Cu_3BiS_3 electrode. The differential capacity (dQ/dV) plots of the Cu_3BiS_3 electrode for first, second, and third cycle are explored (Figure 2c). Unlike the second and third cycle, a reduction peak at 1.1 V can be observed due to the formation of the SEI. After the second cycle, the dQ/dV curves mostly overlap, indicating the good reversibility of the electrochemical reaction. This result is consistent with that of CV test. In addition, to improve the conductivity of Cu_3BiS_3,[35] the electrochemical performance test is investigated after Cu_3BiS_3 mixing with graphite. Figures S4–S9 (Supporting Information) show the detailed microstructures and characteristics of Cu_3BiS_3 containing graphite. The cycling performance of graphite is shown in Figure S10 (Supporting Information), indicating that graphite does not contribute much to the capacity. As shown in Figure 2d, the Cu_3BiS_3 electrode delivers a discharge capacity of 422.7 mA h g^{-1} at 0.1 A g^{-1} after 200 cycles. The initial capacity fading is mainly attributed to the irreversible reaction caused by K^+ insertion, like the decomposition of electrolyte and the formation of unstable SEI layer.[36] Figure 2e shows the rate performance of the Cu_3BiS_3 electrode at various current densities from 0.1 to 10 A g^{-1}. At current densities of 0.1, 0.2, 0.5, 1, 2, 4, 6, 8, and 10 A g^{-1}, the discharge capacities of Cu_3BiS_3 are 377.1, 326.3, 288.5, 259.2, 203.9, 112.2, 68.9 and 58.3 mA h g^{-1}, respectively.

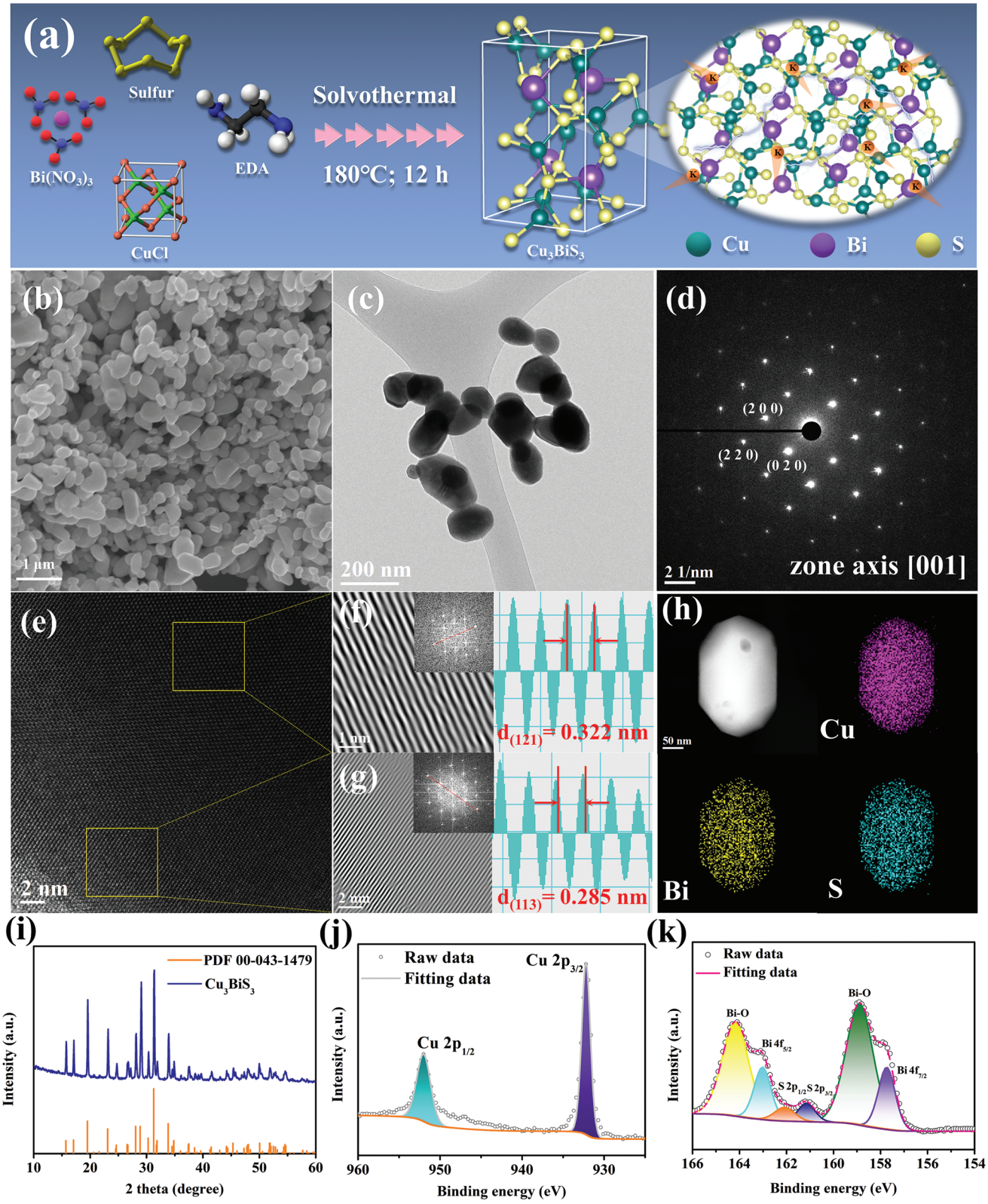

Figure 1. a) Schematic illustration of the preparation process, b) SEM image, c) TEM image, d) SAED pattern, e) HRTEM image, f,g) FFT patterns and the inverse fast Fourier transformations (IFFTs), h) elemental mapping images, i) XRD pattern, high-resolution XPS spectrum of j) Cu 2p and k) Bi 4f and S 2p of as-prepared Cu_3BiS_3 NPs.

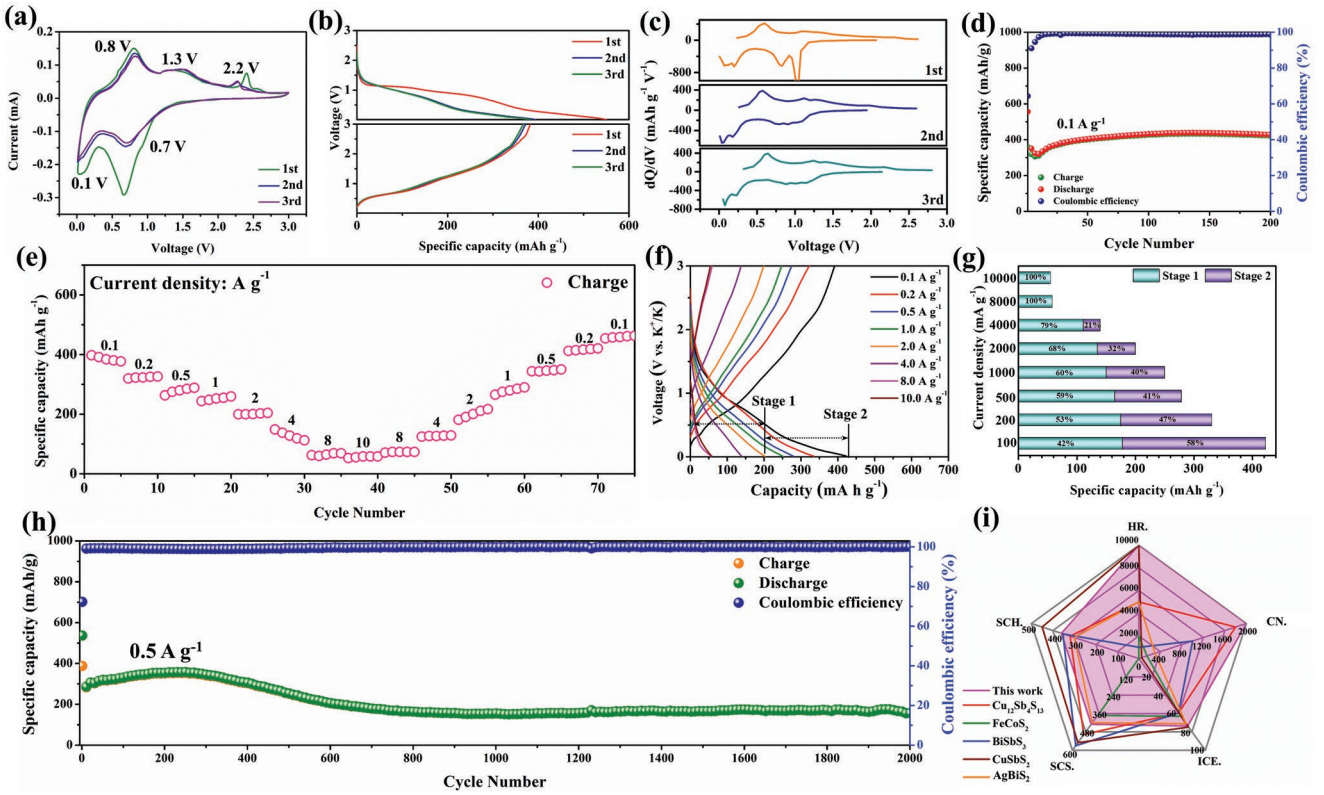

Figure 2. a) CV curves at 0.1 mV s^{-1}. b) GCD curves and c) differential capacity plots of the initial 3 cycles. d) Cycling performance at 0.1 A g^{-1}. e) Rate performance and f) GCD curves at various current density. g) Discharge capacity from the I plateau and II plateau. h) Cycling performance at 0.5 A g^{-1}. i) Comparison of initial Coulombic efficiency (ICE), highest current rate (HR), slow-rate specific capacity at 100 mA g^{-1} (SCS), high-rate specific capacity at 500 mA g^{-1} (SCH), and cycle number (CN) with previous works.

When the current density returns to 0.1 A g^{-1}, the capacity of 426.8 mA h g^{-1} can be recovered, demonstrating its impressive rate performance. As shown in Figure 2f, the corresponding GCD curves at the different scan rates can be divided into two stages: (I) the conversion reaction of Cu_3BiS_3 and K_xS_y, and the alloying reaction of Bi. (II) the conversion reaction from K_xS_y to K_2S and the alloying reaction from K_3Bi_2 to K_3Bi. The capacity contributed by each reaction mechanism in Figure 2g will be calculated based on the plateau. At the higher current density (≧8 A g^{-1}), the capacity is only contributed by stage I, which may be due to polarization,[37,38] which means that the high limiting current density for Cu_3BiS_3 electrodes is about 8 A g^{-1}. Although stage I contributes almost 100% of the discharge capacity at the higher current density, both of stage I and II contribute capacity at a high current density of 4 A g^{-1}, indicating the Cu_3BiS_3 electrode still has good rate performance (Figure 2g). In addition, to further reveal the K^+ storage kinetics of the Cu_3BiS_3 electrode, CV measurements at different scan rates (0.2–5 mV s^{-1}), galvanostatic intermittent titration technique (GITT) tests and in situ electrochemical impedance spectroscopy (EIS) measurements were performed (Figures S11 and S12, Supporting Information). The results confirm pseudocapacitive-controlled behavior and fast ion transfer. And, it can be observed that the charge transfer resistance decreased because of the conversion reaction after K^+ insertion, then the charge transfer resistance further decreased during the first charge process due to complete depotassiation and the decomposition of the irreversible SEI layer (Figure S11f, Supporting Information).[39] Cu_3BiS_3 is a ternary chalcogenide-based material with longer cycle performance. As shown in Figure 2h, Cu_3BiS_3 half-cell was performed at 0.5 A g^{-1} for 2000 cycles to further illustrate the cycling stability of material. The reversible capacity of Cu_3BiS_3 can still be maintained at 158.8 mA h g^{-1}, and the average Coulombic efficiency is as high as 99.5%. Furthermore, Cu_3BiS_3 electrode exhibits high rate capability (10 A g^{-1}) and excellent long-cycle stability (2000 cycles). The long-term cycle performance of the previously reported ternary chalcogenide-based (such as $CuSbS_2$, $FeCoS_2$, $BiSbS_3$, and $AgBiS_2$) has not exceeded 1000 cycles, except $Cu_{12}Sb_4S_{13}$ (Figure 2i).[4,40–43]

To confirm the phase transition of the Cu_3BiS_3 electrode during the charging/discharging process, ex situ XRD analysis was performed at six different potentials, as shown in **Figure 3**a and Table S1 (Supporting Information). First, it can be observed that some fixed peaks are attributed to Al foil, and partially oxidized CuO . The peaks of pristine Cu_3BiS_3 disappear gradually after the insertion of K^+ ions. When discharging to 0.9 V, the conversion and alloying reactions are initiated, some small peaks associated with Cu (PDF#00-004-0836), Bi (PDF#00-044-1246), K_2S_5 (PDF#00-026-1336) and KBi_2 (PDF#04-010-8776) were detected. The formation of KBi_2 can be attributed to the further reaction of Bi with K^+. Then, the peaks at 17.3° and 30.5° appear when discharging to 0.4 V, indicating that K_2S_5

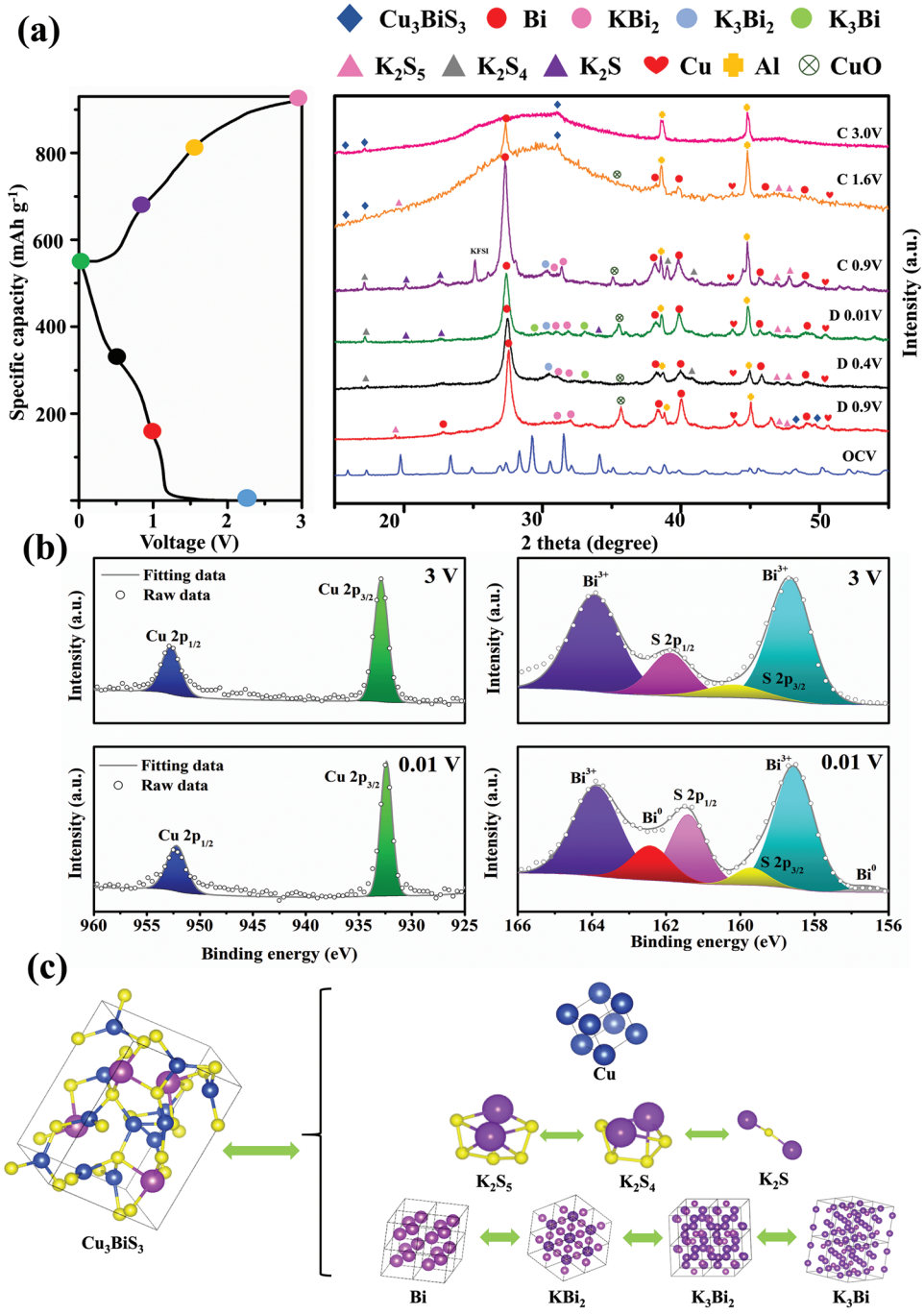

Figure 3. a) Ex situ XRD pattern of Cu_3BiS_3 at different depotassiation/potassiation states. b) Ex situ high-resolution XPS analysis at fully discharged and charged states. c) Schematic illustration of the K^+ storage mechanism of the Cu_3BiS_3 electrode during charging/discharging process.

converts into K_2S_4 (PDF#00-030-0992) and K^+ ions react with the KBi_2 alloy to form K_3Bi_2 (PDF#04-019-3118). When discharged to 0.01 V, the peaks of K_3Bi (PDF#04-007-3496) and K_2S (PDF#00-023-0496) can be observed. During the subsequent charging process, it can be observed that the intensity of the peak at 17.14° increases after charging to 0.9 V, corresponding to the conversion reaction of K_2S forming K_2S_4. Meanwhile, the peaks of K_3Bi at 29.5° and 33.1° disappear, and the peak intensity of K_3Bi_2 at 30.5° increases, indicating that the dealloying reaction by reappeared K_3Bi_2. When further charging to 1.6 V, the peaks of K_2S_4 at 17.3° and K_3Bi_2 at 30.5° disappear, which can be attributed to the conversion reaction from K_2S_4 to K_2S_5, and the dealloying reaction from K_3Bi_2 to Bi. Finally, the diffraction peaks at 15.3°, 17.2°, and 31.1° can be observed at the fully charged state (3 V), indicating the formation of Cu_3BiS_3. This result indicates that the reaction is reversible. Ex situ XPS can provide chemical speciation of Cu, Bi, and S, and further identify the phases transformation in the fully discharged and

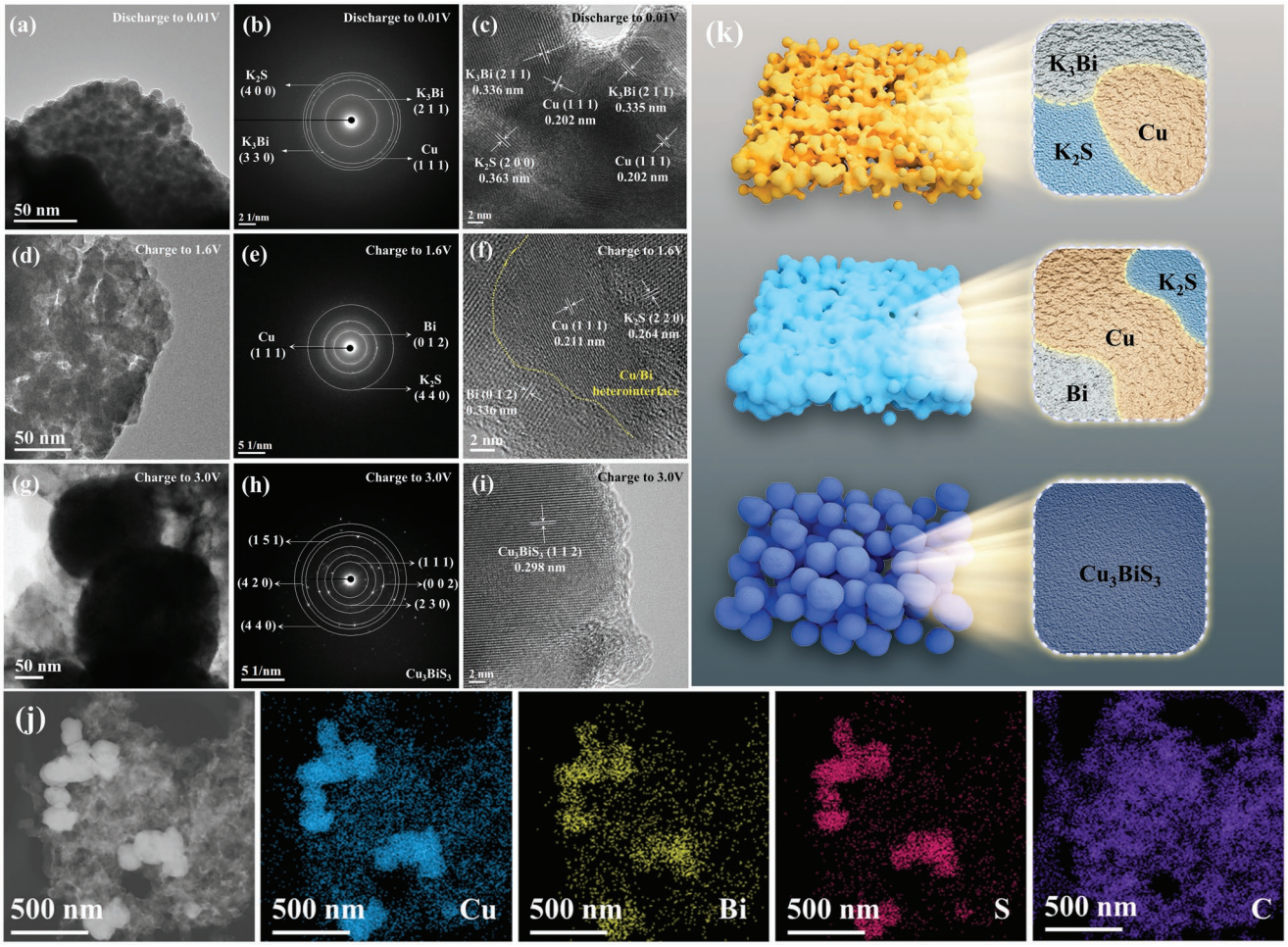

Figure 4. Low magnification TEM images, SAED patterns and HRTEM images of the cycled Cu_3BiS_3: a–c) discharged to 0.01 V, d–f) charged to 0.6 V, g–i) charged to 3.0 V. j) EDS elements mapping of Cu_3BiS_3 after charging to 3.0 V. k) Schematic illustration of morphological and phase evolution of the Cu_3BiS_3 electrode at various potassiation/depotassiation state. (Orange: discharging to 0.01 V, light blue: charging to 1.6 V, dark blue: charging to 3 V).

charged states (Figure 3b). First, in the spectra of Cu 2p at 0.01 V, the binding energy is smaller than that at 3 V, which is related to the metallic Cu phase.[44] Furthermore, the peak of Bi^0 at 156.6 eV and 162.4 eV can be observed at 0.01 V, which can be attributed to the alloying reaction. However, the peak of Bi^0 disappears at 3 V, indicating the transformation reaction between Bi^{3+} and metallic Bi^0.[45] In the S 2p spectra, it can be clearly observed that the peaks of S $2p_{1/2}$ and S $2p_{3/2}$ are shifted to the right at 0.01 V, which reveals the formation of K_2S.[46] Therefore, the potassium ion storage mechanism of Cu_3BiS_3 can be proposed based on the above results (Figure 3c), as follows:

Conversion reaction

$$5Cu_3BiS_3 + 6K^+ + 6e^- \leftrightarrow 15Cu + 5Bi + 3K_2S_5 \quad (1)$$

$$4K_2S_5 + 2K^+ + 2e^- \leftrightarrow 5K_2S_4 \quad (2)$$

$$K_2S_4 + 6K^+ + 6e^- \leftrightarrow 4K_2S \quad (3)$$

Alloying reaction

$$2Bi + K^+ + e^- \leftrightarrow KBi_2 \quad (4)$$

$$KBi_2 + 2K^+ + 2e^- \leftrightarrow K_3Bi_2 \quad (5)$$

$$K_3Bi_2 + 3K^+ + 3e^- \leftrightarrow 2K_3Bi \quad (6)$$

Furthermore, the morphological evolution accompanying the phase change during discharge–charge is further demonstrated by ex situ TEM, HRTEM and SAED measurements at different potential states. At the discharged state (0.01 V), **Figure 4**a shows uniformly dispersed small grain NPs, representing that the grain size of Cu_3BiS_3 changed from large grain size of about 50–100 nm to small grain size of about 10 nm after K^+ insertion. The corresponding SAED patterns in Figure 4b confirm that the discharge products are Cu, K_3Bi, and K_2S. And, Figure 4c clearly shows the lattice fringes of 0.202, 0.335, and 0.363 nm, corresponding to the (111) plane of Cu, the (211) of K_3Bi and the (200) plane of K_2S. When charging to 1.6 V, it can be found that the originally uniform NPs become irregular in size, but the grain size is still smaller than that of the original Cu_3BiS_3 (Figure 4d). Figure 4e shows that the corresponding SAED pattern can be indexed into the (111) plane of the Cu phase, the (012) plane of the Bi phase, and (440) planes of the K_2S phase. Notably, in addition to the lattice fringes at 0.264 nm,

corresponding to the (220) plane of K_2S, the heterostructure interface between Cu (111) (the spacing: 0.211 nm) and Bi (012) (the spacing: 0.336 nm) can be clearly observed (Figure 4f). This heterointerface may suppress the shuttle effect. In particular, when fully charging to 3 V, the small-grained NPs changed back to large-grained NPs (Figure 4g). The corresponding SAED pattern and HRTEM image confirm that the material reversibly forms Cu_3BiS_3 after full depotassiation (Figure 4h,i). Based on the above results, it is consistent with ex situ XRD results. And, the EDS mapping results of Cu_3BiS_3 still maintain large-grained NP, and shows a uniform distribution of Cu, Bi, and S elements (The carbon element is super p). This result is the same as for pristine Cu_3BiS_3 (Figure 4j). Through TEM analyses, the electrochemical and morphological evolution of Cu_3BiS_3 is illustrated in Figure 4k. From a macroscopic point of view, the size changes of Cu_3BiS_3 NPs are roughly divided into three major types: ≈10 nm (orange), ≈20 nm (light blue), and ≈100 nm (dark blue). During the charge and discharge process, the morphology changes of Cu_3BiS_3 electrode: dark blue (open circuit voltage) → orange (0.01 V) → light blue (1.6 V) → dark blue (3 V). In addition, from a microscopic point of view, Cu_3BiS_3 is first converted into Cu, Bi, and K_xS_y. Finally, they will be deconverted into Cu_3BiS_3. These results confirm the dual reversible reaction of the Cu_3BiS_3 electrode.

The structural evolution can be more intuitively reflected through SEM and TEM images of different cycles, as shown in **Figure 5**. After charging to 1.6 V, Figure 5a1 shows that the irregular NPs are tightly aggregated. The corresponding HRTEM pattern shows the lattice fringes of 0.266, 0.211, and 0.337 nm, corresponding to the (220) plane of K_2S, the (111) plane of Cu, and the plane of Bi (012), respectively (Figure 5a2). Most importantly, it can be clearly observed the Cu/Bi heterostructure interface. Subsequently, due to the insertion of potassium ion, the NPs with large grain size relative to the size at 1.6 V appeared (Figure 5a3). The corresponding HRTEM pattern shows the lattice fringes of 0.296 nm, corresponding to the (112) plane of Cu_3BiS_3. In particular, the grain size is similar to that of unreacted Cu_3BiS_3, meaning that both the phase transition and the morphology are reversible during the initial charge/discharge process. After the five cycles, the material still formed small grain size of the irregular NPs at 1.6 V (Figure 5b1). In addition, the products of the conversion reactions are composed of K_2S, Cu, and Bi, and the Cu/Bi heterostructure interface can be clearly observed (Figure 5b2). At the fully charged state, the large-grained NPs were formed again, implying the morphological reversibility during the potassiation/depotassiation process (Figure 5b3). However, in terms of Cu_3BiS_3, although the grain size of the intermediate phase is small at discharged state, it will convert to large grain size of the products at full charged state. The Cu_3BiS_3 electrode morphology evolution of 20 cycles is similar to that of the first cycle. Notably, the same situation can be observed after 50 cycles (Figures S13 and S14, Supporting Information). Even after 2000 cycles, Cu_3BiS_3 can convert to large grain size at a full charged state (Figure 5h).

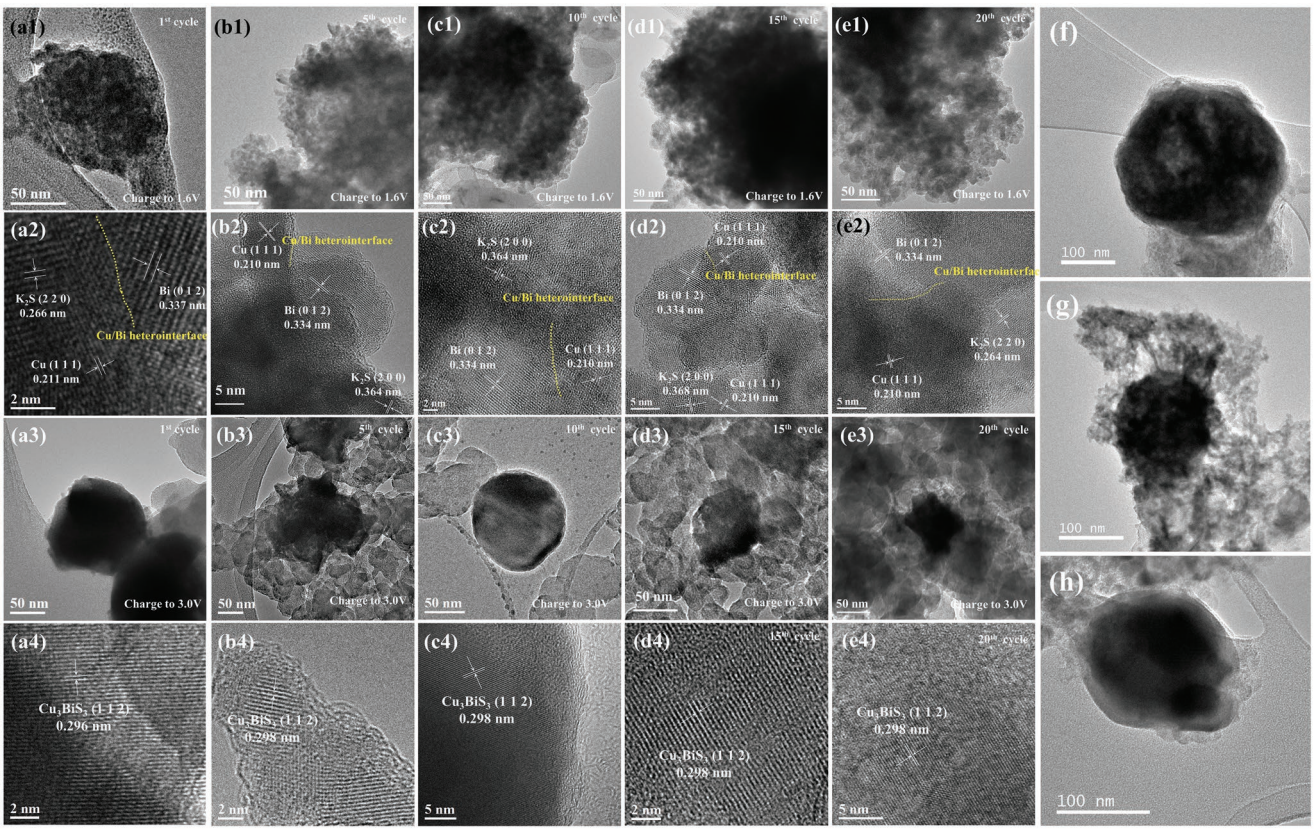

Figure 5. TEM and HRTEM images of the Cu_3BiS_3 electrodes after charged to 1.6 V, and 3 V at the a) 1st, b) 5 th, c) 10 th, d)15 th, and e) 20th cycle. TEM images of the Cu_3BiS_3 electrodes after f) 500, g) 1500 and h) 2000 cycles.

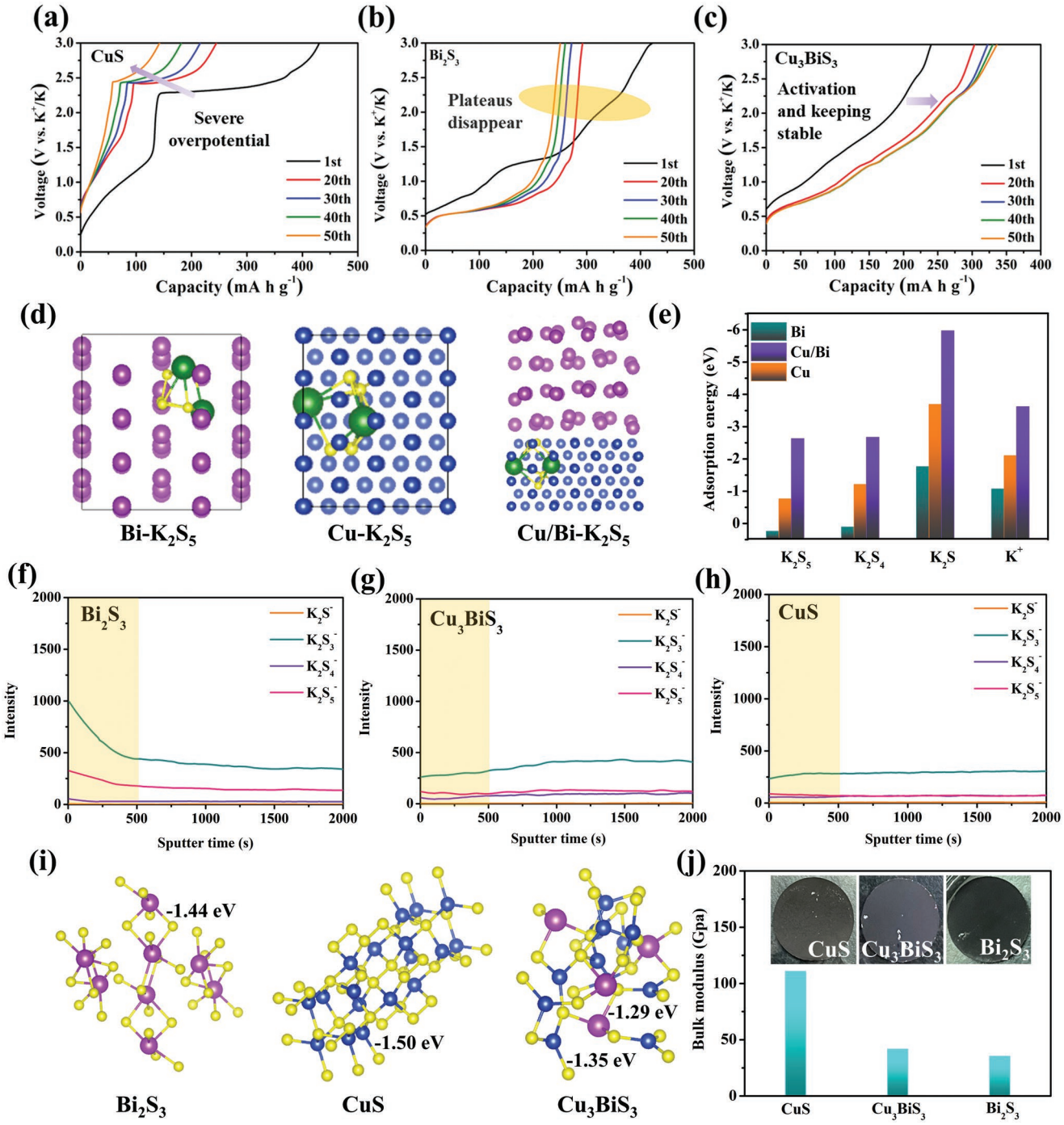

Figure 6. Charge curves of a) CuS, b) Bi_2S_3 and c) Cu_3BiS_3 under current density of 0.5 A g^{-1} for the 1st, 20th, 30th, 40th, 50th cycle. d) Optimized conformation of K_2S_5 absorption on the surface of the Bi, Cu and Cu/Bi heterostructure interface. e) Calculated adsorption energies of K_2S_5, K_2S_4, K_2S, and K^+ on Bi, Cu and Cu/Bi heterostructure interface. Negative-mode ToF-SIMS depth profiles of various fragments for K_xS_y in fully charged f) Bi_2S_3, g) Cu_3BiS_3 and h) CuS electrodes after 20 cycles. i) The Cu—S and Bi—S bonds energy of Bi_2S_3, CuS, and Cu_3BiS_3. j) The bulk modulus of CuS, Cu_3BiS_3, and Bi_2S_3.

After repeated potassiation/depotassiation process, the Cu_3BiS_3 nanomaterials can remain the phase reversibility and the morphological reversibility at the same time, which can be great benefit to the cycling stability of Cu_3BiS_3.

We explore whether the Cu_3BiS_3 electrode is more stable for potassium-ion battery than binary analog (Bi_2S_3 and CuS). The XRD pattern, SEM image, and cycle performance of Bi_2S_3 and CuS are shown in Figures S15–S17 (Supporting Information). The charging curves of Cu_3BiS_3, Bi_2S_3 and CuS at the 1st, 20th, 30th, 40th, and 50th cycles are investigated (**Figure 6**a–c). During the first cycle, the potential plateaus of the three samples were clearly evident. However, both the Bi_2S_3 and CuS electrodes are

obviously unstable after the first cycle. It can be found that the plateau of Bi_2S_3 electrode gradually disappears at 2.2 V, and the CuS electrode suffers severe overpotential. Obviously, in the GCD curves of the Cu_3BiS_3 electrode, the potential plateaus are still obvious after 50 cycles, indicating that the Cu_3BiS_3 electrode is relatively stable during the potassiation/depotassiation process. In addition, the adsorption capability of sulfur-based materials plays an important role in reducing the shuttle effect.[47,48] To understand the interaction between the material and K_xS_y, the DFT theoretical calculations are carried out to further demonstrate the adsorption capability (Table S2, Supporting Information). Figure 6d shows the optimized configuration of K_2S_5 on Bi, Cu, and Cu/Bi heterostructure interface surfaces. The K_2S_5 adsorption energy of Cu/Bi heterostructure interface is -2.63 eV, which is greater than that of Cu-K_2S_5 (-0.76 eV) and Bi-K_2S_5 (0.24 eV). It shows that the Cu/Bi heterostructure interface has stronger anchoring capability toward K_2S_5. Then, it can be found that the K_2S_5 and K_2S_4 adsorption energy of Bi are 0.24 eV and 0.11 eV, indicating that K_2S_5 and K_2S_4 are not adsorbed easily on the Bi surface (Figure 6e and Figure S18, Supporting Information). The results confirm that both of Cu and Cu/Bi heterostructure interface can avoid the shuttle effect caused by the dissolution of polysulfides in the electrolyte. However, the Cu/Bi heterostructure interface has better anchoring capability toward polysulfides than Cu. Next, ToF-SIMS was performed on the surface of the Cu_3BiS_3 and Bi_2S_3 and CuS electrodes after 20 cycles (Figure 6f–h). At the beginning of the beam sputtering, the difference between the Bi_2S_3, CuS, and Cu_3BiS_3 electrodes can be clearly observed. The intensity of K_xS_y on the surface of the Bi_2S_3 electrode is higher than that on the CuS and Cu_3BiS_3 electrodes. And, it weakens gradually after 500 s, indicating that the polysulfides are dissolved in the electrolyte during cycling. This result is consistent with the DFT result. Additionally, we also use DFT calculations to investigate why Cu_3BiS_3 has the advantages of phase reversibility and morphology reversibility, while Bi_2S_3 and CuS do not. According to the previous report by Guo et al., the lattice softening effect may be attributed to the low bond energy.[49] Therefore, the Bi—S and Cu—S bond energies of CuS, Bi_2S_3 and Cu_3BiS_3 were analyzed by DFT to investigate the relative elasticity of the materials. Figure 6i shows that the Bi—S bond energy of Bi_2S_3 is -1.44 eV, the Cu—S bond energy of CuS is -1.50 eV and the Cu—S and Bi—S bond energies of Cu_3BiS_3 are -1.35 eV and -1.29 eV, respectively. It can be found that Cu—S bond energy of CuS has the highest, which means that CuS has a larger energy barrier to rebuild its bonds, indicating that its elastic deformation range is small. Next, the elastic deformation ability of Cu_3BiS_3, Bi_2S_3, and CuS was observed through bulk modulus. Figure 6j and Table S3 (Supporting Information) show that the bulk modulus value of CuS is larger than that of Bi_2S_3 and Cu_3BiS_3, indicating that the CuS material has relatively large stress and strong rigidity. On the contrary, the bulk modulus values of Cu_3BiS_3 and Bi_2S_3 are small, and they are more elastic than CuS materials. In addition, it can be found from the inset that there are no cracks on the surface of the Bi_2S_3 and Cu_3BiS_3 electrodes after 20 cycles, and it can be speculated that the elastic deformation ability of the material is beneficial to rebuild its structure.

This electrochemical reconstruction property, like a self-healing material, has a repair function after damage and maintains the original integrity of material. In the natural world, it is well known that organisms have the ability to repair themselves. Regardless of skin and bones, they can continue to regenerate after external damage. However, unlike the ability to regenerate and reshape in nature, batteries are made of inanimate synthetic materials such as polymers and inorganic materials, and most of the materials are unable to return to their original structure when subjected to huge the volume expansion of ion insertion/extraction, which in turn affects battery performance. The irreversible reactions often lead to decrease the capacity and the cycling stability in battery. The degradation of battery performance is the interaction of different processes related to the thermodynamic, chemical, and mechanical instability of the material. Therefore, through self-healing materials, the mechanical stability of the materials and the stability of the material structure can be improved without preventive steps (such as artificial interfaces, coatings, additives, etc.). Previous methods cannot completely prevent chemical/physical damage to the material. On the contrary, self-healing materials can restore their original function. Next, in terms of bond energy, the Cu—S and Bi—S bond energies of Cu_3BiS_3 are lower, so that Cu_3BiS_3 does not need a large energy to rebuild, which proves that Cu_3BiS_3 has high elastic recovery.[50] Finally, Cu_3BiS_3 has an elastic structure due to the small bulk modulus value, so that the electrode is not easy to crack during the potassiation/depotassiation process. Like the high tough of rubber, its modulus is very low and it won't crack easily. This is similar to the result that we found no crack phenomenon on the surface of Cu_3BiS_3 electrode after potassiation/depotassiation. It can be speculated that a material with self-healing properties can stabilize its own structure without a protective layer (such as rGO and dopamine). The advantages of self-healing materials can extend cycle life and improve material stability. In addition, when charged to 1.6 V, it can be found that Bi and Cu NPs are uniformly distributed (Figure 5a2–e2). However, Bi_2S_3 and CuS electrode has obvious aggregation problem after 50 cycles (Figure S19, Supporting Information), further resulting in a longer diffusion path and lower potassium storage kinetics. In contrast, the Cu precipitation in the process of charge and discharge is beneficial to uniformly disperse Bi particles and ensure a short diffusion path of potassium ions. We further speculate that Cu can be used as a separator to avoid the serious aggregation of Bi particles due to repeated volume expansion/contraction during the charge and discharge process. Coupled with the high conductivity of Cu, which can improve the kinetics of Cu_3BiS_3.[51] Finally, although Bi is not easy to adsorb polysulfides (based on the results of calculations and TOF-SIMS tests), the Cu/Bi heterostructure interface has the ability to adsorb polysulfides, confirming that the Cu/Bi heterostructure interface can suppress the shuttle effect, which is beneficial to the reversible reactions of Cu_3BiS_3. Moreover, by calculating the K_xS_y adsorption energy of Cu/Bi heterostructure interface, it can be found that the interaction between Cu/Bi heterostructure interface and K_xS_y is high, which means that S in Cu_3BiS_3 will not be easy to precipitate during the charging and discharging process. This is why Cu_3BiS_3 has reversible properties. The self-healing of Cu_3BiS_3 electrode proposed here is expected to serve as a rational design for advanced electrode materials. Therefore, the feasibility of PIBs and PIHCs with Cu_3BiS_3 anode is further investigated.

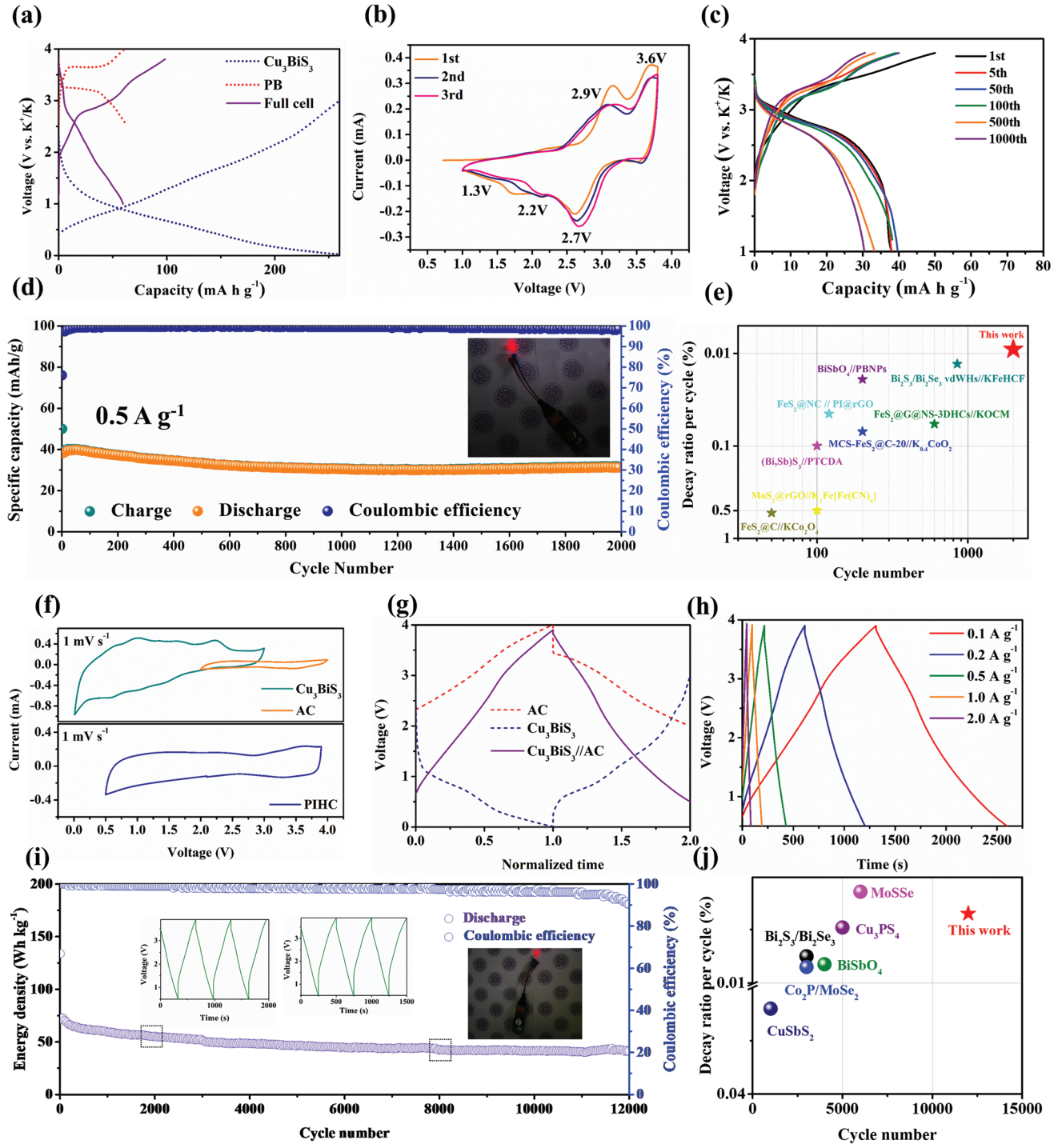

Figure 7. a) GCD curves of the PB half cell, Cu_3BiS_3 half cell, and Cu_3BiS_3//PB full cell. b) CV curves at a scan rate of 1 mV s^{-1}. c) GCD curves and d) long-term cycling performance at 2500 mA g^{-1} of the Cu_3BiS_3//PB full cell. e) Comparison of the decay ratio per cycle and cycling stability of the full cells in previous report. f) CV curves and g) normalized GCD curves of the AC half cell, Cu_3BiS_3 half cell and the Cu_3BiS_3//AC PIHC. h) GCD curves of the Cu_3BiS_3//AC PIHC at various current density. i) Long-term cycling performance of the Cu_3BiS_3//AC PIHC at 2500 mA g^{-1}. Insets present the pseudocapacitive profile and a digital picture while lighting a red LED bulb. j) Comparison of the decay ratio per cycle and cycling stability of the PIHCs in previous report.

The K-ion full cell is based on the schematic diagram in **Figure 7**, using a PB cathode, to verify the practical feasibility of the Cu_3BiS_3 anode. The structural and electrochemical characterization of the PB cathode is shown in Figures S20 and S21 (Supporting Information). In addition, Figure 7a shows that the potassium storage performance of the Cu_3BiS_3//PB full

cell are tested between 1.0 and 3.8 V, and it can be observed that Cu_3BiS_3//PB full cell delivers the initial discharge/charge capacities of 58.6 and 98.3 mA h g^{-1}, respectively. Furthermore, the overlapping peaks in the CV curves indicate the reversibility of the Cu_3BiS_3//PB full cell (Figure 7b). The rate capability of Cu_3BiS_3//PB full cells was investigated (Figure S22, Supporting Information). Based on the mass of cathode, it can deliver a discharge capacity of 55.3, 47.6, 40.9, 36.8, 33.8 and 31.4 mA h g^{-1} at 0.1, 0.2, 0.4, 0.6, 0.8 and 1 A g^{-1}, respectively. The corresponding GCD curves at the different scan rates are shown in Figure S22b (Supporting Information). The similar shapes of the charge–discharge curves indicate good reversibility. Based on Figure S22a (Supporting Information), the high energy density of 90.7 Wh kg^{-1} and the power density up to 1527.2 9 W kg^{-1} can be achieved (Figure S23, Supporting Information). The GCD curves of the Cu_3BiS_3 electrode in Figure 7c show the potential plateaus are still obvious after 1000 cycles, indicating that the Cu_3BiS_3//PB full cell is relatively stable. Furthermore, the Cu_3BiS_3//PB full cell exhibits a good cycling stability of 31.67 mA h g^{-1} after 200 cycles at 0.5 A g^{-1} (Figure 7d). The CE can reach around 99% after a few cycles. Interestingly, when fully charged, the Cu_3BiS_3//PB full cell can successfully light up a red light-emitting diode (LED), as shown in Figure 7d. Based on the reported results of the full cells using conversion-type anode, the electrochemical performance of Cu_3BiS_3//PB full cell was compared (Figure 7e and Table S4, Supporting Information). Cu_3BiS_3//PB full cell has a relatively long-term cycle performance and slow decay rate.[4,8,46,52–56] Therefore, the above results imply that the Cu_3BiS_3 electrode is a very promising anode for PIBs applications.

Moreover, PIHC with the advantages of both batteries and supercapacitors was assembled using Cu_3BiS_3 as anode and commercial activated carbon as the cathode (denoted as Cu_3BiS_3//AC).[57] The electrochemical performance of the AC cathode was estimated before assembling and testing the PIHC (Figure S24, Supporting Information). Figure 7f,g shows the CV and GCD curves of Cu_3BiS_3 half-cell, AC half-cell, and Cu_3BiS_3//AC full-cell with mass ratios of 1.1:1. The CV curve of the half-cell determines the working voltage range (0.5–3.9 V) of Cu_3BiS_3//AC full-cell. Furthermore, the GCD of Cu_3BiS_3//AC full cell is not ideal triangle, implying a hybrid energy storage mechanism. Furthermore, kinetics analysis was also carried out (Figure S25, Supporting Information). The CV curves at different rate show no obvious overpotential shifting, indicating that the pseudocapacitive in Cu_3BiS_3// AC full cells is highly dominated. Next, Figure 7h and Figure S26 (Supporting Information) show that Cu_3BiS_3//AC can deliver energy densities of 68.1, 63.5, 57.0, and 49.7 Wh kg^{-1} at 0.1, 0.2, 0.5, 1 A g^{-1}, respectively. Even at a high current density of 2 A g^{-1}, Cu_3BiS_3//AC PIHC can still deliver an energy density of 41.0 Wh kg^{-1}. When the current density returned to 1 A g^{-1}, the Cu_3BiS_3//AC PIHC still delivers an energy density of 49.7 Wh kg^{-1} and can be stably cycled for 25 cycles, showing excellent reversibility of Cu_3BiS_3//AC. Figure S27 (Supporting Information) shows the Ragone plot of the Cu_3BiS_3//AC PIHC. The power density up to 3516.2 W kg^{-1} can be achieved at the energy density of 41 Wh kg^{-1}. Furthermore, the cycling performance of Cu_3BiS_3//AC PIHC was investigated at the current density of 1 A g^{-1} (Figure 7i). Compared with the initial value, the Cu_3BiS_3//AC PIHC can maintain about 58% capacity retention after 12 000 cycles. The insets of Figure 7i are the voltage curves for approximately 2000 and 8000 cycles, and show that the Cu_3BiS_3//AC PIHC can easily light up a red LED. Notably, it can be observed that the voltage curves at different cycles have similar shapes, indicating extraordinary cycling stability and reversibility. Therefore, based on the above results, Figure 7j shows that cycle performance and decay rate of Cu_3BiS_3//AC PIHC are longer and slower than those of conversion-type based other PIHCs, such as: Bi_2S_3/Bi_2Se_3//AC, $CuSbS_2$//AC, $BiSbO_4$//AC, $Co_2P/MoSe_2$//AC, MoSSe//AC, and Cu_3PS_4//AC.[8,41,46,58–60]

3. Conclusion

In summary, we successfully demonstrated the self-healing properties of the Cu_3BiS_3 anode material. The new idea for the electrochemical reconstruction of electrodes can provide a clearer and more comprehensive Cu_3BiS_3 electrode morphological change. Electrochemical reconstruction is a morphological change process determined by synergistic effects between the electrode materials. We can affirm that morphological change affects the final electrochemical performance. In this work, the morphological change and related electrochemical properties of the Cu_3BiS_3 electrode are explored in detail. We confirm Cu_3BiS_3 with excellent electrochemical performance through the following important results: i) in the electrochemical mechanism, the Cu_3BiS_3 electrode first undergoes electrochemical activation after the insertion of potassium ions, which in turn leads to the electrochemical reconstruction of Cu_3BiS_3; ii) small-grained intermediates transformed can avoid the agglomeration of Bi NPs and effectively adsorb K_xS_y intermediates, thereby improving the reversibility of the conversion reaction and maintaining excellent kinetics; iii) DFT calculation (the adsorption energy of K_xS_y, bond energy Cu_3BiS_3, and elastic modulus) provided the basic theory of Cu_3BiS_3 in the process of large-grain/small-grain transformation. In particular, Cu_3BiS_3 NPs can transform between large and small grain sizes, which is different from other anode materials with electrochemical reconstruction, where the size of nanomaterial becomes smaller during cycling. Through the TEM results of different cycle, it can be found that the phenomenon of morphology changes in the Cu_3BiS_3 electrode occurs continuously, indicating the self-healing process of Cu_3BiS_3 is quite reversible. Therefore, this concept can reduce the capacity decay rate, improve the reactivity of the electrode, and then maintain the cycling stability of the electrode. Based on the results of this study and the process of electrochemical reconstruction, the mechanism for the effect of electrochemical reconstruction on electrochemical performance can be further explored in depth. Alternatively, an innovative controllable system may also be developed in the future, through external pressure (electrical conditions) or internal environment (additives) to achieve regulation of electrochemical reconstruction/non-autonomous self-healing systems. Therefore, electrochemical reconstruction of the self-healing materials provides a great strategy for applications in a wide range of energy storage devices.

4. Experimental Section

Materials: Iron(II) chloride tetrahydrate ($FeCl_2{\cdot}4H_2O$, 98%), thioacetamide (98%), and ethylenediamine (99%) were purchased from Alfa Aesar. Potassium metal (98%), 1,2-dimethoxyethane (DME, anhydrous 99.5%), NaCMC (average MW ≈700 000), potassium hexacyanoferrate (II) trihydrate ($K_4Fe(CN)_6{\cdot}3H_2O$, 98.5%), potassium chloride (KCl, 99%), ethanol (99.5%), thiourea (99%), copper sulfate ($CuSO_4$, 98%), and copper(I) chloride (CuCl, 99%), bismuth(III) nitrate pentahydrate ($Bi(NO_3)_3{\cdot}5H_2O$, 99.5%), sulfur powder (99%), and ethylene glycol (EG, 99%) were purchased from Sigma Aldrich. Potassium citrate (99%) and ascorbic acid (99.7%) were purchased from Honeywell. Potassium bis(fluorosulfonyl)imide (KFSI, 97%) was purchased from Combi-Blocks. Glass fiber was purchased from Advantec. Super-P, graphite, PVDF, and coin cell CR2032 were purchased from Shining Energy. Active carbon was purchased from Kuraray Chemical Company. Deionized water was produced by a Milli-Q Direct pure water system.

Synthesis of Cu_3BiS_3 NPs: Cu_3BiS_3 NPs were obtained by a facile hydrothermal method. 150 mg of CuCl was dissolved in 10 mL of ethylenediamine (solution A), and then 225 mg of $Bi(NO_3)_3{\cdot}5H_2O$ was dissolved in solution A to give a dark blue solution. 48 mg of sulfur powder was added to 10 mL of ethylenediamine (solution B). Slowly drop solution B into solution A and stir until uniform. The above solution was transferred to a 50 mL Teflon-lines autoclave, sealed in a stainless steel autoclave and placed in an oven to heat at 180 °C for 12 h. The precipitate was collected by centrifugation and washed three times with ethanol.

Synthesis of Cu_3BiS_3 Containing Graphite: 60 mg of Cu_3BiS_3 NPs and 20 mg of graphite were placed in a stainless steel ball-milling jar, and the mixture was milled at 200 rpm for 24 h under argon protection using a high-energy mechanical ball mill (RETSCH PM100). The weight ratio of grinding balls/mixture powder was 222:1.[61]

Synthesis of CuS Nanowires: 0.48 mmol of $CuSO_4{\cdot}5H_2O$ and 0.96 mmol of thiourea were dissolved in 20 mL and 30 mL of DI water, respectively. The two solutions were slowly mixed and stirred for 15 min before being transferred to a 100 mL Teflon-lines autoclave, sealed in a stainless steel autoclave, and placed in an oven for 2 h at 170 °C. The black precipitate was collected by centrifugation and washed several times with ethanol and DI water.[62]

Synthesis of Bi_2S_3 Nanotubes: 0.75 mmol of $Bi(NO_3)_3{\cdot}5H_2O$ was dissolved in 15 mL of ethylene glycol, called solution A. 1.125 mmol of thioacetamide was added to 15 mL of ethylene glycol, referred to as solution B. Solution A was dropped into solution B and stirred for 30 min, and heated to 60 °C for 24 h. The product was collected by centrifugation and washed several times with DI water and ethanol.[4]

Synthesis of Prussian Blue: Prussian blue (PB) was synthesized by coprecipitation method. Solution A was formed by 5 mmol of $FeCl_2{\cdot}4H_2O$ in 100 mL of ethanol. Solution B was formed by dissolving 5 mmol $K_4Fe(CN)_6{\cdot}3H_2O$, 10 mmol potassium citrate, 15 g potassium chloride, and 0.5 g ascorbic acid in 100 mL of DI water. The solution A was slowly dropped into the solution B, and maintained for 12 h under stirring to form a uniformly dispersed dark blue suspension. The product was collected by centrifugation, washed three times with DI water, and finally dried in a vacuum oven.[63]

Materials Characterizations: X-ray diffraction patterns were recorded on an X-ray diffractometer (XRD, Bruker, D8 ADVANCE) with Cu-Kα radiation. X-ray photoelectron spectroscopy (ULVAC-pH PHI Quantera II) identified the chemical composition and valence state of the samples. The microstructure and morphology of the samples were observed using a scanning electron microscope (SEM, HITACHI-SU8010) equipped with an energy X-ray spectrometer (EDS) and a transmission electron microscope (TEM, JEOL, ARM200F) with an accelerating voltage of 200 kV. Raman spectroscopy was performed using a Raman spectrometer (LABRAM HR 800 UV). Thermogravimetric analysis was performed using a thermogravimetric analyzer (TA, Q50) in the atmosphere with a temperature ramp rate of 10 °C min^{-1} and a temperature range of 25–800 °C.

Electrochemical Measurements: The anode electrode was prepared by dispersing the as-prepared Cu_3BiS_3, super P, and NaCMC in DI water at a ratio of 7:2:1 to form the slurry. The slurry was coated on copper foil and heated to 80 °C in an argon gas furnace to dry for 1 h and remove the solvent. The average mass loading of active materials on the electrodes is about 0.8–1 mg cm^{-2}. Glass fiber was used as the separator, 4 M KFSI in DME was used as the electrolyte, and potassium foil was used as the counter electrode for half cell. The electrochemical performance of the prepared electrodes was tested using a CR2032 type button cell. CV and EIS curves were obtained on a Bio-Logic-Science instrument VMP3 workstation. The constant current charge–discharge test was performed by NEWARE CT-4000 with a working window of 0.01 to 3.0 V. The cathode electrode of the full cell was prepared by dispersing the prepared PB, CNT and NaCMC in DI water in a ratio of 7:2:1 to form a slurry. The slurry was coated on aluminum foil and dried by heating to 80 °C in an argon furnace tube for 1 h to remove the solvent. The average mass loading of active materials on the electrodes is about 1.1–1.2 mg cm^{-2}. Before assembling the full cell, the cathode and anode were charged and discharged for 10 cycles at current densities of 120 and 500 mA g^{-1}. The mass ratio of positive and negative active materials is 4:1. The cathode electrode of the hybrid capacitor is made by dispersing AC, super P and PVDF in NMP in a ratio of 8:1:1 to form a slurry. And it was heated to 150 °C in a furnace tube with argon for 2 h to remove the solvent. The average mass loading of active material on the electrode is about 0.9 mg cm^{-2}. Before assembling the hybrid capacitor, the anode was charged and discharged for 3 cycles at a current density of 100 mA g^{-1}. The mass ratio of positive and negative active materials is 1.1:1.

Computational Methods: All the DFT calculations were carried out using Dmol^3 code of Materials Studio 2020 (Accelrys Software Inc.) on the Hefei advanced computing center.[64] Each compute node includes two 2nd Gen AMD EPYC(TM) Rome 7702 64-core, 128-thread processors, and 256G DDR4 3200 MHz eight-channel RAM. The VASP code was built and configured using hybrid openMPI/openMP parallelization environment. In a typical geometry optimization process, each self-consistent field (SCF) of electronic steps takes about 60 s. The exchange and correlation energies were determined with the Perdew, Burke, and Ernzerhof (PBE) functional within the generalized gradient approximation (GGA).[65] The DFT semi-core pseudo potentials (DSPP) core treatment is implemented for relativistic effects, which replaces core electrons by a single effective potential and introduce some degree of relativistic correction into the core. Moreover, the double numerical plus polarization (DNP) is chosen as the basis set.[66] Among the basis sets provided by dmol3 code, the DNP basis set has the best accuracy and highest computational cost. A thermal smearing of 0.005 Ha (1 Ha = 27.21 eV) to the orbital occupation is applied to speed up electronic convergence. The convergence tolerance of electronic structure and geometry optimization are 1×10^{-7} Ha, 5×10^{-4} Ha $Å^{-1}$, respectively. The global orbital cutoff is 5.6 Å. The adsorption energy (E_{ad}) was calculated through Equation (1)

$$E_{ad}(M) = E_{sys} - E_M - E_s \quad (1)$$

where E_{sys}, E_M, and E_s are the DFT calculated energies of the adsorption systems, an isolated molecule, and surface, respectively. The bond energy (E_b) were calculated through Equation (2)

$$E_b = E_{formation}/n_b \quad (2)$$

where $E_{formatoin}$, and n_b are the formation energy per cell, and the number of bonds per cell. The elastic constants of bulk cell were calculated using Voigt-Reuss-Hill (VRH) approximation.[67–69]

Supporting Information

Supporting Information is available from the Wiley Online Library or from the author.

Acknowledgements

This work was supported by the financial support from the 2030 Cross-Generation Young Scholars Program by Ministry of Science and Technology, Taiwan (MOST 111-2628-E-007 -008). H.-Y.T. also acknowledges the financial support of National Tsing Hua University, Taiwan, through the grant of 111QI030E1.

Conflict of Interest

The authors declare no conflict of interest.

Data Availability Statement

The data that support the findings of this study are available from the corresponding author upon reasonable request.

Keywords

batteries, electrochemical reconstruction, hybrid capacitors, potassium ions, self-healing

Received: January 3, 2023
Revised: February 24, 2023
Published online:

[1] J. L. Lian, Y. Wu, Y. C. A. Guo, Z. Y. Zhao, Q. H. Zhang, Y. Hou, L. X. Chen, B. Lu, X. H. Pan, Z. Z. Ye, J. G. Lu, *Chin. Chem. Lett.* **2022**, *33*, 3931.
[2] Y. Guo, R. Khatoon, J. Lu, Q. He, X. Gao, X. Yang, X. Hu, Y. Wu, J. Lian, Z. Li, Z. Ye, *Carbon Energy* **2021**, *3*, 841.
[3] Y. Tian, J. Lu, H. Tang, X. Wang, L. Zhang, P. Hu, L. Zhou, Y. Wang, Y. Guo, R. Khatoon, Q. Zhang, Q. He, Y. He, M. Qiu, Y. Hou, Z. Ye, *Chem. Eng. J.* **2021**, *422*, 130054.
[4] J. Wang, L. Fan, Z. Liu, S. Chen, Q. Zhang, L. Wang, H. Yang, X. Yu, B. Lu, *ACS Nano* **2019**, *13*, 3703.
[5] H. Zhang, Y. Cheng, Q. Zhang, W. Ye, X. Yu, M.-S. Wang, *ACS Nano* **2021**, *15*, 10107.
[6] C. Huang, A. Xu, G. Li, H. Sun, S. Wu, Z. Xu, Y. Yan, *Small* **2021**, *17*, 2100685.
[7] H. Shan, J. Qin, Y. Ding, H. M. K. Sari, X. Song, W. Liu, Y. Hao, J. Wang, C. Xie, J. Zhang, *Adv. Mater.* **2021**, *33*, 2102471.
[8] Y. -Y. Hsieh, H. -Y. Tuan, *Energy Storage Mater.* **2022**, *51*, 789.
[9] S. Zhang, F. Ling, L. Wang, R. Xu, M. Ma, X. Cheng, R. Bai, Y. Shao, H. Huang, D. Li, *Adv. Mater.* **2022**, *34*, 2201420.
[10] L. Mezzomo, C. Ferrara, G. Brugnetti, D. Callegari, E. Quartarone, P. Mustarelli, R. Ruffo, *Adv. Energy Mater.* **2020**, *10*, 2002815.
[11] E. R. Ezeigwe, L. Dong, R. Manjunatha, M. Tan, W. Yan, J. Zhang, *Nano Energy* **2021**, *84*, 105907.
[12] H. Chen, Z. Wu, Z. Su, S. Chen, C. Yan, M. Al-Mamun, Y. Tang, S. Zhang, *Nano Energy* **2021**, *81*, 105654.
[13] Z. Xu, J. Yang, T. Zhang, Y. Nuli, J. Wang, S.-i. Hirano, *Joule* **2018**, *2*, 950.
[14] X. Jiao, J. Yin, X. Xu, J. Wang, Y. Liu, S. Xiong, Q. Zhang, J. Song, *Adv. Funct. Mater.* **2021**, *31*, 2005699.
[15] T. Munaoka, X. Yan, J. Lopez, J. W. To, J. Park, J. B. H. Tok, Y. Cui, Z. Bao, *Adv. Energy Mater.* **2018**, *8*, 1703138.
[16] J. Zhu, Y. Wu, X. Huang, L. Huang, M. Cao, G. Song, X. Guo, X. Sui, R. Ren, J. Chen, *Nano Energy* **2019**, *62*, 883.
[17] S. Haghighat-Shishavan, M. Nazarian-Samani, M. Nazarian-Samani, S. H. Hosseini-Shokouh, T. Maschmeyer, K.-B. Kim, *Chem. Eng. J.* **2022**, *435*, 134965.
[18] H. He, D. Huang, Q. Gan, J. Hao, S. Liu, Z. Wu, W. K. Pang, B. Johannessen, Y. Tang, J.-L. Luo, *ACS Nano* **2019**, *13*, 11843.
[19] P. Xiong, J. Wu, M. Zhou, Y. Xu, *ACS Nano* **2019**, *14*, 1018.
[20] D. Li, X. Ren, Q. Ai, Q. Sun, L. Zhu, Y. Liu, Z. Liang, R. Peng, P. Si, J. Lou, *Adv. Energy Mater.* **2018**, *8*, 1802386.
[21] S. Ni, J. Zhang, J. Ma, X. Yang, L. Zhang, X. Li, H. Zeng, *Adv. Mater. Interfaces* **2016**, *3*, 1500340.
[22] S. Ni, B. Zheng, J. Liu, D. Chao, X. Yang, Z. Shen, J. Zhao, *J. Mater. Chem. A* **2018**, *6*, 18821.
[23] K.-T. Chen, Y.-C. Yang, L.-M. Lyu, M.-Y. Lu, H.-Y. Tuan, *Nano Energy* **2021**, *88*, 106233.
[24] M. Morales-Gallardo, J. E. Pascoe-Sussoni, C. Delesma, X. Mathew, F. Paraguay-Delgado, J. Muñiz, N. Mathews, *J. Alloys Compd.* **2021**, *886*, 158447.
[25] Z. Wang, K. Yu, S. Gong, H. Mao, R. Huang, Z. Zhu, *ACS Appl. Mater. Interfaces* **2021**, *13*, 16246.
[26] S.-C. Lu, M.-C. Hsiao, M. Yorulmaz, L.-Y. Wang, P.-Y. Yang, S. Link, W.-S. Chang, H.-Y. Tuan, *Chem. Mater.* **2015**, *27*, 8185.
[27] X. Jia, E. Zhang, X. Yu, B. Lu, *Energy Technol.* **2020**, *8*, 1900987.
[28] Y. Wei, W. Hou, P. Zhang, R. A. Soomro, B. Xu, *Chin. Chem. Lett.* **2022**, *33*, 3212.
[29] K.-T. Chen, S. Chong, L. Yuan, Y.-C. Yang, H.-Y. Tuan, *Energy Storage Mater.* **2021**, *39*, 239.
[30] G. Suo, J. Zhang, D. Li, Q. Yu, M. He, L. Feng, X. Hou, Y. Yang, X. Ye, L. Zhang, *J. Colloid Interface Sci.* **2020**, *566*, 427.
[31] B. Sheng, L. Wang, H. Huang, H. Yang, R. Xu, X. Wu, Y. Yu, *Small* **2020**, *16*, 2005272.
[32] J. Huang, X. Lin, H. Tan, B. Zhang, *Adv. Energy Mater.* **2018**, *8*, 1703496.
[33] K. Lei, C. Wang, L. Liu, Y. Luo, C. Mu, F. Li, J. Chen, *Angew. Chem.* **2018**, *130*, 4777.
[34] C. Shen, G. Song, X. Zhu, D. Wang, L. Huang, Z. Sun, Y. Wu, *Nano Energy* **2020**, *78*, 105294.
[35] Y. Son, N. Kim, T. Lee, Y. Lee, J. Ma, S. Chae, J. Sung, H. Cha, Y. Yoo, J. Cho, *Adv. Mater.* **2020**, *37*, 2003286.
[36] M. Cai, H. Zhang, Y. Zhang, B. Xiao, L. Wang, M. Li, Y. Wu, B. Sa, H. Liao, L. Zhang, *Sci. Bull.* **2022**, *67*, 933.
[37] G. Y. Ma, X. Xu, Z. Y. Feng, C. J. Hu, Y. S. Zhu, X. F. Yang, J. Yang, Y. T. Qian, *Nano Res.* **2020**, *13*, 802.
[38] Y. Chen, L. B. Ma, X. P. Shen, Z. Y. Ji, A. H. Yuan, K. Q. Xu, S. A. Shah, *J. Alloys Compd.* **2019**, *801*, 90.
[39] S. H. Yang, S. K. Park, Y. C. Kang, *Nano-Micro Lett.* **2021**, *13*, 9.
[40] C.-B. Chang, K.-T. Chen, H.-Y. Tuan, *J. Colloid Interface Sci.* **2022**, *608*, 984.
[41] X. Chen, N. Cheng, L. Zhang, G. Xiang, Y.-L. Ding, Z. Liu, *J. Alloys Compd.* **2021**, *861*, 158458.
[42] X. Ren, D. Yu, L. Yuan, Y. Bai, K. Huang, J. Liu, S. Feng, *J. Mater. Chem. A* **2020**, *8*, 15058.
[43] Y. Cao, Y. Zhang, H. Chen, S. Qin, L. Zhang, S. Guo, H. Yang, *Adv. Funct. Mater.* **2022**, *32*, 2108574.
[44] Y. Wang, D. Chao, Z. Wang, J. Ni, L. Li, *ACS Nano* **2021**, *15*, 5420.
[45] C.-H. Chang, K.-T. Chen, Y.-Y. Hsieh, C.-B. Chang, H.-Y. Tuan, *ACS Nano* **2022**, *16*, 1486.
[46] B. Li, Z. He, J. Zhao, W. Liu, Y. Feng, J. Song, *Small* **2020**, *16*, 1906595.
[47] L. Sun, Y. Liu, J. Xie, L. Fan, J. Wu, R. Jiang, Z. Jin, *Chem. Eng. J.* **2023**, *451*, 138370.
[48] X. Long, Z.-H. Luo, W.-H. Zhou, S.-K. Zhu, Y. Song, H. Li, C.-N. Geng, B. Shi, Z.-Y. Han, G.-M. Zhou, *Energy Storage Mater.* **2022**, *52*, 120.
[49] S. Guo, H. Li, Y. Lu, Z. Liu, X. Hu, *Energy Storage Mater.* **2020**, *27*, 270.

[50] H. Shan, J. Qin, J. Wang, H. M. K. Sari, L. Lei, W. Xiao, W. Li, C. Xie, H. Yang, Y. Luo, *Adv. Sci.* **2022**, *9*, 2200341.
[51] Z. Tong, T. Kang, Y. Wu, F. Zhang, Y. Tang, C.-S. Lee, *Nano Res.* **2022**, *15*, 7220.
[52] S. Chong, L. Sun, C. Shu, S. Guo, Y. Liu, W. A. Wang, H. K. Liu, *Nano Energy* **2019**, *63*, 103868.
[53] Y. Du, W. Weng, Z. Zhang, Y. He, J. Xu, J. Sun, J. Liao, J. Bao, X. Zhou, *ACS Mater. Lett.* **2021**, *3*, 356.
[54] B. Chen, J. Ding, X. Bai, H. Zhang, M. Liang, S. Zhu, C. Shi, L. Ma, E. Liu, N. Zhao, *Adv. Funct. Mater.* **2022**, *32*, 2109899.
[55] H. Wu, S. Lu, S. Xu, J. Zhao, Y. Wang, C. Huang, A. Abdelkader, W. A. Wang, K. Xi, Y. Guo, *ACS Nano* **2021**, *15*, 2506.
[56] Z. Zhang, L. Duan, Y. Xu, C. Zhao, J. Bao, J. Shen, X. Zhou, *J. Energy Chem.* **2022**, *73*, 126.
[57] Y. Yuan, Y. Lu, B.-E. Jia, H. Tang, L. Chen, Y.-J. Zeng, Y. Hou, Q. Zhang, Q. He, L. Jiao, J. Leng, Z. Ye, J. Lu, *Nano-Micro Lett.* **2019**, *11*, 42.
[58] Y. Wang, W. Kang, X. Pu, Y. Liang, B. Xu, X. Lu, D. Sun, Y. Cao, *Nano Energy* **2022**, *93*, 106897.
[59] J. Gao, G. Wang, Y. Liu, J. Li, B. Peng, S. Jiao, S. Zeng, G. Zhang, *J. Mater. Chem. A* **2020**, *8*, 13946.
[60] S.-F. Ho, H.-Y. Tuan, *Chem. Eng. J.* **2022**, *51*, 789.
[61] W.-C. Lin, Y.-C. Yang, H.-Y. Tuan, *Energy Storage Mater.* **2022**, *51*, 38.
[62] B. Zhang, X.-W. Gao, J.-Z. Wang, S.-L. Chou, K. Konstantinov, H.-K. Liu, *J. Nanosci. Nanotechnol.* **2013**, *13*, 1309.
[63] X.-D. He, Z.-H. Liu, J.-Y. Liao, X. Ding, Q. Hu, L.-N. Xiao, S. Wang, C.-H. Chen, *J. Mater. Chem. A* **2019**, *7*, 9629.
[64] B. Delley, *J. Chem. Phys.* **2000**, *113*, 7756.
[65] J. P. Perdew, K. Burke, M. Ernzerhof, *Phys. Rev. Lett.* **1996**, *77*, 3865.
[66] B. Delley, *J. Chem. Phys.* **1990**, *92*, 508.
[67] D. Chung, W. Buessem, *J. Appl. Phys.* **1967**, *38*, 2010.
[68] H.-J. Yang, C.-Y. Chen, F.-W. Yuan, H.-Y. Tuan, *J. Phys. Chem. C* **2003**, *117*, 21955.
[69] J. Tang, C.-Y. Wang, F. Xiu, A. J. Hong, S. Chen, M. Wang, C. Zeng, H.-J. Yang, H.-Y. Tuan, C.-J. Tsai, *Nanotechnology* **2010**, *21*, 505704.